

RESEARCH

Supervised topological data analysis for MALDI imaging applications

Gideon Klaila^{1*†}, Vladimir Vutov^{2†} and Anastasios Stefanou^{1†}

*Correspondence:

klailag@uni-bremen.de

¹Institute for Algebra, Geometry, Topology and their Applications (ALTA); Department of Mathematics, University of Bremen, 28359 Bremen, Germany
Full list of author information is available at the end of the article

[†]Equal contributor

Abstract

Background: Matrix-assisted laser desorption/ionization imaging mass spectrometry (MALDI IMS) displays significant potential for applications in cancer research, especially in tumor typing and subtyping. Lung cancer is the primary cause of tumor-related deaths, where the most lethal entities are adenocarcinoma (ADC) and squamous cell carcinoma (SqCC). Distinguishing between these two common subtypes is crucial for therapy decisions and successful patient management.

Results: We propose a new algebraic topological framework, which obtains intrinsic information from the MALDI data and transforms it to reflect topological persistence in the data. Our framework has two main advantages. First, the topological persistence helps us to distinguish the signal from noise. Second, it compresses the MALDI data, which results in saving storage space, and also optimizes the computational time for further classification tasks. We introduce an algorithm that performs our topological framework and depends on a single tuning parameter. Furthermore, we show that it is computationally efficient. Following the persistence extraction, logistic regression and random forest classifiers are executed based on the resulting persistence transformation diagrams to classify the observational units into binary class labels, describing the lung cancer subtypes. Further, we utilized the proposed framework in a real-world MALDI data set, and the competitiveness of the methods is illustrated via cross-validation.

Conclusion: Our empirical experiments demonstrate that the proposed algebraic topological framework obtains the necessary (spectral) information and produces the highest classification results in a shorter computational time compared to the non-extracted counterparts. Specifically, the random forest algorithm enhances its overall classification performance on average by above 1% based on the persistence transformation diagrams.

Keywords: Imaging mass spectrometry; Persistent homology; Persistence transformation; Merge Tree; Logistic Regression; Random Forest

Background

Matrix-assisted laser desorption/ionization imaging mass spectrometry (MALDI IMS), also known as MALDI Imaging, is a label-free tool for spatially furnishing molecular weight information of compounds like proteins, peptides, and many others (see, e.g., [1], [2]). Provided a thin biological sample (usually a tissue section, e.g., in [3], [4]), MALDI collects mass spectra at multiple discrete positions within the biological sample. As a result, an image is obtained where each spatial spot

presents a mass spectrum ([5]). The latter depicts the relative abundances of ionizable molecules with a significant number of mass-to-charge ratio (m/z) values, ranging from a couple of hundreds to a few tens of thousands of m/z values (see [3], [5], [6]). MALDI has been demonstrated to be a valuable instrument for many pathological applications (for more details, see [7] or [8]), which is possible because of its feasibility in examining formalin-fixed paraffin-embedded (FFPE) tissue samples. In other words, the MALDI tool allows analyses of multiple tumor cores across many patients by aggregating them in a single tissue microarray (TMA) (cf. [2]). As discussed in [9], "the pathological diagnosis of a tumor found in a tissue specimen, including the determination of the tumor origin and genetic subtype" ([9]) is essential for adequate treatment of patients. This study reports our findings on a MALDI data set based on two lung cancer (LC) subtypes.

As pointed out by several studies (e.g., in [4], [6] and [10]), a plain approach to discovering associative m/z values relies upon the idea of identifying significant signal peaks, also known in the literature as peak detection. Focusing on the relevant peaks, one can neglect those highly associated with noise, as acknowledged in [5]. Then, significant peaks are assumed to provide information for discriminating mass spectra from different cancer subtypes (see, among others, in [11] and [12]). A comparison of different peak-detection algorithms has been reported in [13]. Furthermore, in [14], a more recent and novel approach proposes to incorporate an isotope pattern ([15]) around the chosen peaks, which can boost the peak detection methodology.

Other methods aim to extract "characteristic spectral patterns (CSP)" from MALDI-IMS data (cf. [4], [9]). Namely, these methods combine spectral similarities from different correlated spectral features into a lower dimensional subspace from data. Afterward, classification models are performed on the extracted feature vectors to classify data units into class labels, i.e., the tumor types or subtypes. Some other frameworks tend to perform a feature selection first. Then, based on the selected features, such frameworks execute supervised classification methods to classify observational units into response labels based on the selected features (e.g., [16]). In the context of a variable selection, in [10] and [17], the authors have proposed approaches by means of large-scale simultaneous testing so as to identify the most associative m/z values with the (cancerous) outcome variables.

The usual challenge modeling methods face is a significant amount of spectral data. As more and more data are being gathered, it becomes increasingly more challenging to analyze the data efficiently with short computational times. Topological data analysis (TDA) is a contemporary scientific area that arose from diverse works in applied topology and computational geometry (see [18], [19]). TDA offers an algebraic way of reducing the dimensionality of data sets and extracting essential features in short computational times.

TDA is a relatively novel field of data analysis, and more theoretical work needs to be done to improve the methods (cf. [20]). Even so, TDA has been successfully employed in various fields of science, e.g., in physics, chemistry, and bio-medicine ([21]), as well as in oncology (see [22], [23]). Motivated by these approaches, this study's objective is to propose a novel framework based on the algebraic topology of MALDI imaging to get improved classification results in a shorter computational time.

In the context of MALDI, one can take advantage of TDA by filtering out the most relevant part of the data, namely the peak-related information. We hypothesize that the importance of a peak increases with its relative height, also known as topological "persistence". Accordingly, low persistent peaks are more likely to be noise.

A general approach to determining a peak's persistence is the upper-level set filtration, where each peak corresponds to a topological feature. These topological features are tracked from their appearance until they merge with a larger feature. This way of analyzing the data is fast in its computational time, but it has a significant drawback. While tracking the persistence of each peak, one loses the information about their positions, which is paramount to carrying out data analysis applications. For example, in the context of MALDI-related studies, the locations of the biomarkers (cf. [4], [10]) are relevant information for the analysis. To circumvent this limitation, we introduce a different analysis method: the persistence transformation (cf. [24]). The proposed approach keeps track of each peak's position while determining its persistence.

Topological Data Analysis

MALDI data structure

The first step of our approach is to transform the input MALDI data in order to reflect the topological persistence. For the convenience of notation, we will explain the data structure through words and give more precise notation in the preceding section. MALDI-IMS data sets are commonly stored in an $n \times p$ matrix, where each data entry corresponds to an intensity value of the detected particles of a certain mass-to-charge ratio (m/z value). Usually, mass spectra are stored as rows, while every data column corresponds to an intensity plot for a certain m/z value (for more details, see in [9, 25]), i.e., n corresponds to the number of mass spectra, and p is the number of m/z values within a mass spectrum. Furthermore, the data records are non-negative since MALDI data presents information on molecular masses of ionizable molecules (cf. [5]).

In the following, we give a brief overview of the background of persistent homology, leading up to the persistence transformation used in our framework.

Filtration

Let $f : M \rightarrow \mathbb{R}$ be a real-valued function on a compact set, then for $a \in \mathbb{R}$ the upper-level set can be defined as $M_a := \{x \in M \mid f(x) \geq a\}$. Note that $M_a \subseteq M_{a'}$ for any $a > a'$. This yields the "upper-level set filtration" $M_{a_1} \subseteq \dots \subseteq M_{a_i}$ for $a_1 > \dots > a_i \in \mathbb{R}$ (for more details; see Chapter 18 in [20]). In this study, we aim at utilizing the upper-level set filtration instead of the common alternative, i.e., the sublevel set filtration (defined as $M_{\leq a} := \{x \in M \mid f(x) \leq a\}$). Since the latter, filtration detects local minima and tracks them until they merge with other minima. Conversely, the maxima are highly important in MALDI applications because they correspond to the underlying spectral peaks. As mentioned, peaks provide the necessary information to distinguish mass spectra from different cancerous subtypes ([5], [10]). To this end, the upper-level set filtration is of interest in this study since it tracks the local maxima.

Let $x, x' \in M$ with a path-connection, i.e. there exists a continuous function $p : [0, 1] \rightarrow M$ such that $p(0) = x$ and $p(1) = x'$. We denote the image of the map p by

$[x, x']_p$. Then we say that x and x' are path-connected in M_a , and we write $x \sim_a x'$, if there exists a path connection p of x, x' , such that $\forall \hat{x} \in [x, x']_p : \hat{x} \in M_a$, i.e. $f(\hat{x}) \geq a$, for all $\hat{x} \in [x, x']_p$. To track the homology in the upper-level set filtration, we now identify all path-connected points to each other. The degree of the 0-th homology group h_0 is given by $b_0(M_a) = |M_a / \sim_a|$, i.e. the number of different path-connected components in M_a . These components are called "topological features". Henceforth, we refer to a (topological) feature in this pure topological sense, not a feature in a statistical sense, like a covariate or an explanatory variable. Remark that there are no features of dimension one or higher since each data unit (mass spectra; see Figure 5) is represented as a curve.

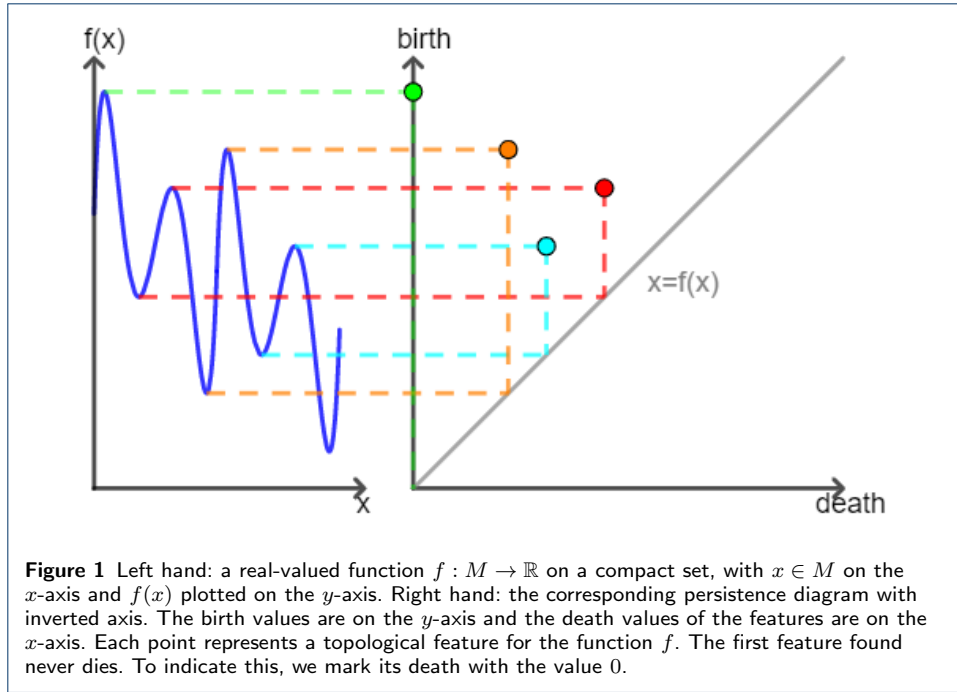
In the upper-level set filtration, a topological feature is detected for x at a^* if and only if $x \in M_{a^*}$ and $\forall x' \in M_{a^*} : x \not\sim_{a^*} x'$, i.e., x is not path-connected to any other element in M_{a^*} . The feature in x merges with another feature in M_{a^+} , if $a^+ = \max\{a \mid x \in M_a \wedge \exists x' \in M_a : x \sim_a x' \wedge f(x') > f(x)\}$, i.e., the largest upper-level set in which the peak gets path-connected to a larger peak. We call a^* the "birth" of the feature, a^+ the "death" of the feature, and $p := a^* - a^+$ the "persistence" of the feature. Since the largest peak (the global maximum) does not merge with any other feature, its death is defined as the global minimum. The induced merging order is according to the "elder rule" (see [26]).

To encode all information about features and their persistence in a meaningful and comparable way, the persistence diagram is utilized. Figure 1 displays an example of the encoding process for the upper-level set filtration. Here, the birth and death axis are swapped since the birth values are always greater or equal to the death values. In this way, all the feature points appear above the diagonal line $x = f(x)$ (cf. Section 4 in [27]). In the persistence diagram, each feature is represented by a point (a^*, a^+) with a multiplicity for similar features. The closer a point is to the diagonal of the diagram $\{(x, f(x) = x) \mid \forall x\}$, the lesser its persistence is and vice versa. For more details of the standard persistence diagram approach, we refer to [28] and [29].

Given two real-valued functions on a compact set $f, g : M \rightarrow \mathbb{R}$, the resulting persistence diagrams $\mathbf{dgm}(f)$ and $\mathbf{dgm}(g)$ can be compared with a suitable metric on the diagrams, e.g., the bottleneck distance (cf. [29], [30]). This metric defines the closeness of persistence diagrams and can also indicate the closeness of the corresponding functions in the sense that if the persistence diagrams are different, the functions are different. In the context of MALDI-IMS data, the persistence diagram can be used as a proxy for distinguishing cancer (sub-)types. The opposite case, that similar persistence diagrams imply similar functions, does not hold, as illustrated in Figure 4.

Persistence transformation

Using persistence homology to track the features and applying the bottleneck distance on the resulting persistence diagrams is a viable way to distinguish functions. However, there is a disadvantage to this approach. While tracking the persistence of each feature in a comprehensible way, its position is not being tracked. Nevertheless, as mentioned above, in data-driven applications, including MALDI Imaging, the position of variables is a required property.



To process the information regarding the positions along with the persistence of peaks, we approach the topological manipulation of the spectral data differently. Instead of creating a point $(a^*, a^+) \in \mathbb{R}^2$ for each feature and displaying it in the persistence diagram, we introduce a new dimension to track the position. For each feature, this approach gives a point $(x, a^*, a^+) \in M \times \mathbb{R}^2$, where $x \in M$ is the position of each peak. We define a pairing function $\mu : M \rightarrow \mathbb{R}$ with $\mu(x) = a$. The value a is defined to be the highest value smaller or equal to $f(x)$, which upper-level set M_a contains a point x' having a greater function value (similarly as in [24]):

$$\mu(x) := \sup\{a \leq f(x) \mid \exists x' \in M_a : f(x') > f(x) \wedge x \sim_a x'\}. \tag{1}$$

For the global maximum \hat{x} the pairing value $\mu(\hat{x})$ is not defined, so we define $\mu(\hat{x}) := \min\{a \in \mathbb{R} \mid \exists x : f(x) = a\}$ instead. Then the birth of a topological feature is given by $a^* = f(x)$, while the death is calculated by $a^+ = \mu(x)$. The persistence p of a point x can now be defined to be

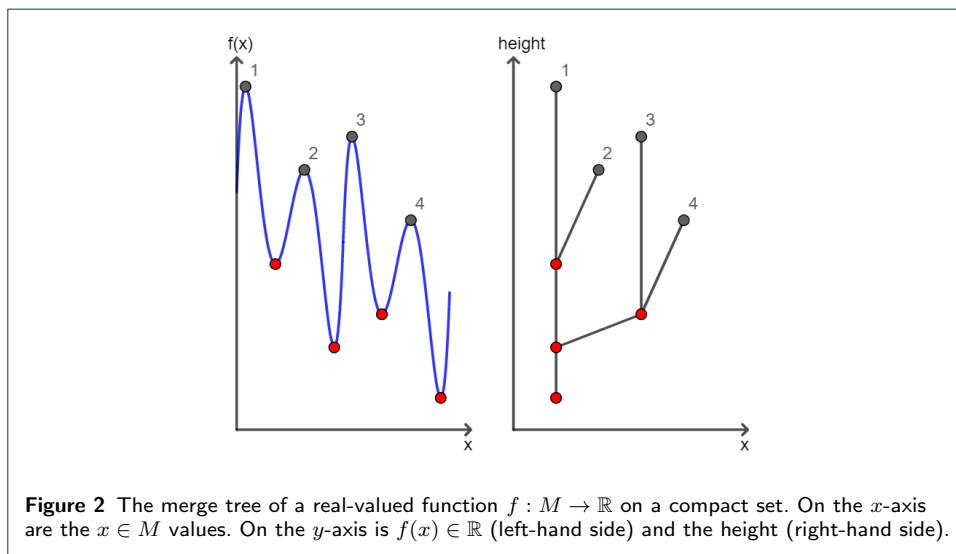
$$p(x) := f(x) - \mu(x) = a^* - a^+.$$

For any point x not being a local maximum there is a local maximum $x' \in M_{f(x)}$ with $f(x') > f(x)$ and $x \sim_{f(x)} x'$. Then the pairing of x is trivial, i.e. $\mu(x) = f(x)$ with the resulting persistence of $p(x) = f(x) - \mu(x) = 0$. Alternatively, for a point x being a local maximum, the pairing is non-trivial, i.e., there is $\mu(x) < f(x)$, which results in a non-zero persistence $p(x) = f(x) - \mu(x) > 0$. This pairing value always corresponds to $f(\tilde{x})$ for a unique local minimum \tilde{x} , i.e.

$$\mu(x) = f(\tilde{x}). \tag{2}$$

The persistence transformation $t : M \rightarrow M \times \mathbb{R}^2$ can then be defined for each $x \in M$ to be $t(x) = (x, f(x), \mu(x)) = (x, a^*, a^+) \in M \times \mathbb{R}^2$. For each $x \in M$, the feature triple $t(x) = (x, a^*, a^+)$ consists of the position, the birth value, and the death value. The storage can be reduced to $3 \cdot m$, with m being the number of peaks, by neglecting the trivial tuples, resulting in the "persistence transformation vector".

Similar to the persistence diagram of the upper-level set filtration, the merging of features in the persistence transformation occurs according to the elder rule (see [26]), i.e., the topological feature with the higher birth value persists when merged to another feature. The process can be illustrated in the corresponding merge tree (e.g., in Figure 2).



Application

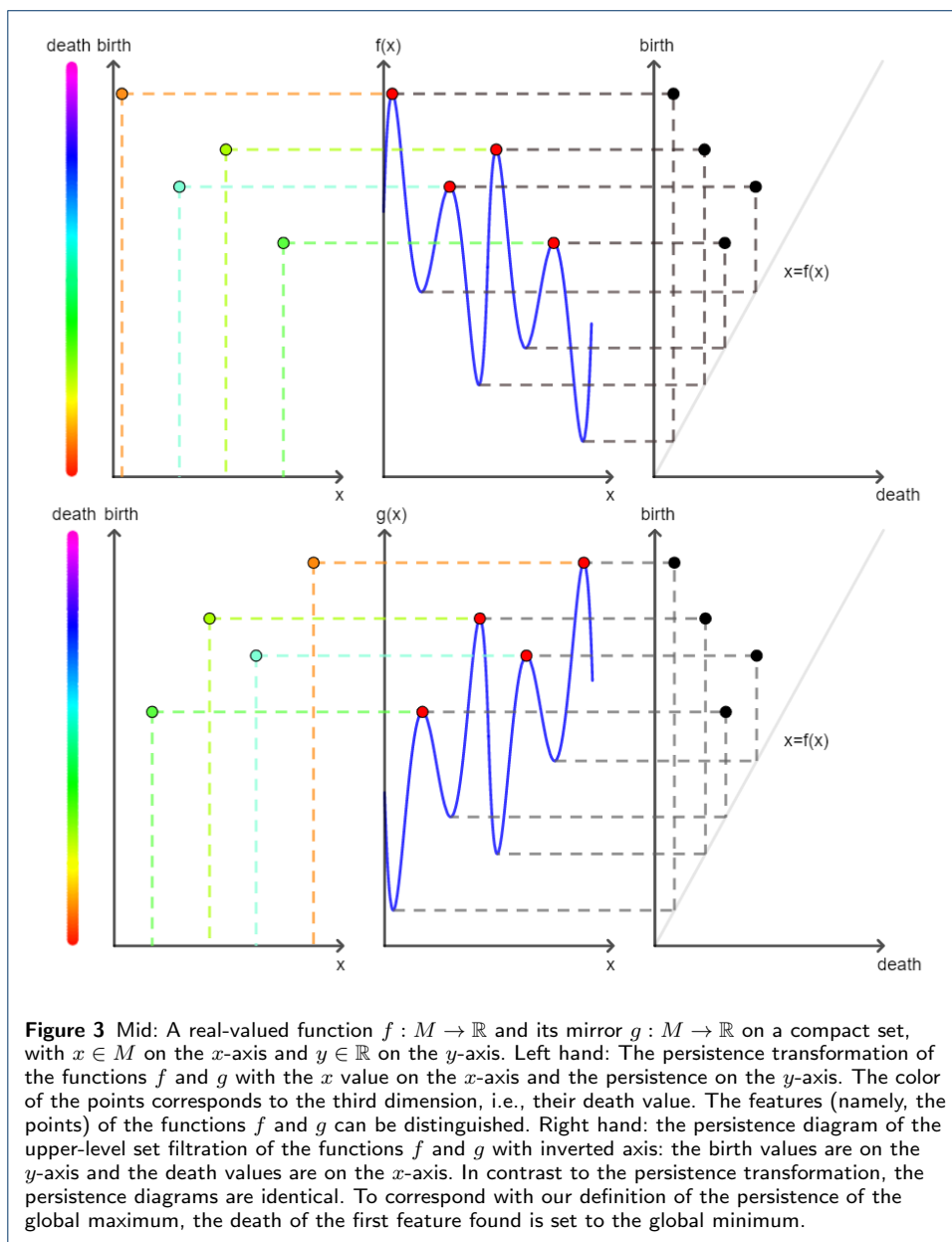
The notion of the persistence transformation is, in theory, a great way to store more topological information about a graph in general. But many applications do not need the whole information provided by the persistence feature. In these cases, the greater dimensionality of the persistence transformation is rather disadvantageous in calculations. This could be evaded by introducing a "reduced persistence transformation", where instead of $t(x) = (x, a^*, a^+)$ only the position and the persistence are stored: $\tilde{t}(x) = (x, a^* - a^+) \in M \times \mathbb{R}$ for $x \in M$. This computational reduction has two benefits. First, it compresses the persistence vector. Second, it can track the persistence of each topological feature and its position.

Another computational improvement for applications can be made by associating low persistent features with noise. By omitting the possible noise by only considering the $k\%$ most persistent features, the accuracy of the analysis can be improved. In addition, reducing the number of stored features might also improve the run-time of subsequent approaches.

Finally, in many applications, there exists a total order on the set M , e.g., if $M \subseteq \mathbb{R}$. This order can be passed to the feature space, such that the elder rule for features with equal birth value can be applied deterministically by using the induced order.

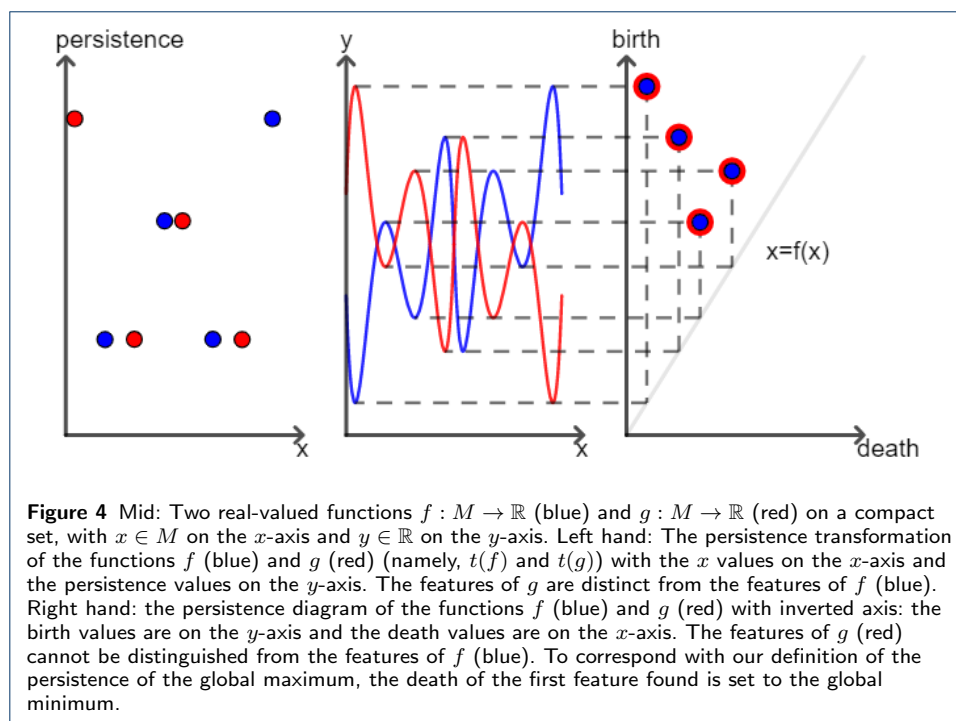
Comparison

The persistence transformation is strictly a better invariant in distinguishing two functions $f, g : M \rightarrow \mathbb{R}$ than the persistence diagram of their 0-dimensional upper-level set filtration. By taking the projection, $p_i((x, a^*, a^+)) = (a^*, a^+)$ of the persistence transformation, the persistence diagram of the upper-level set filtration can be obtained. Hence, all functions that can be distinguished by the persistence diagram can also be distinguished by the persistence transformation. Furthermore, there are cases where the persistence transformation differentiates two functions successfully while the zero dimensional persistence diagram of the upper-level set filtration fails to do so (see Figure 3).



The reduced persistence transformation, on the other hand, is not strictly better than the persistence diagram of the upper-level set filtration. However, there are

cases where the reduced persistence transformation outperforms the persistence diagram (see Figure 4). For MALDI-related applications, one seeks to utilize exactly the advantages that the (reduced) transformation offers. For example, the total height of a peak is less interesting in these applications than the relative height, and the position of the peak can be used to backtrack molecules. To this end, in the MALDI-IMS applications, the reduced persistence transformation performs better in analyzing the spectral data than the persistence diagram of the upper-level set filtration.



The benefit of the persistence transformation can be utilized in different scientific areas where the position of the peaks is of interest (e.g., [31]). In the context of TDA, data analyses generally only work reliably if the applied method is stable, meaning that a slight change in the data (given a suitable metric) only leads to small changes in the numerical results. The persistence diagram has been proven stable (see [29]). Furthermore, there are stability theorems for other topological methods (see [32] and [33]), but to the best of our knowledge, there has not yet been a proven stability theorem for the persistence transformation. This may be done in further work.

Implementation and Analysis of the Algorithm

To analyze the MALDI data set, we implemented a custom-made computer algorithm for the reduced persistence transformation. The recursive algorithm is based on pairing peaks with their unique local minimum (cf. Equation (2)) to determine their persistence. The pseudo code with a detailed analysis by run-time and storage usage is given in the appendix 1, proving the following theorem:

Theorem 1 *The algorithm always terminates and has a complexity of $\sigma(n) + \sigma(m^2)$, where m is the number of peaks for each spectrum and returns all features with their persistence.*

Note that the implementation of the algorithm stores for each feature the tuple $((x, p(x)))$, where $p(x) = a^* - a^+$ is the persistence of the feature. Without the further cost of calculation, the algorithm could calculate the persistence transformation instead of the reduced persistence transformation by storing the triple (x, a^*, a^+) . Furthermore, the algorithm could be adjusted to determine the persistence diagram of the upper-level set filtration instead by storing the tuple (a^*, a^+) .

Supervised methods

The second step of the proposed methodology is to carry out a classification method on the resulting persistences to classify observational units into class labels, i.e., LC subtypes. To do so, we consider two classifiers, logistic regression (LR) and random forest (RF). Note that our goal is to investigate the performance of the proposed topological framework in the context of MALDI modeling, not a benchmark study that compares RF versus LR. For benchmark studies, see, e.g., in [34] and [35].

Logistic Regression

Throughout this manuscript, we assume that observed data on n observational units are expressed in the structure $(Y_i, Z_{i1}, \dots, Z_{ip})$, for $i \in \{1, \dots, n\}$, with a binary response Y_i , describing two LC subtypes, i.e. $Y_i \in \{0, 1\}$. We denote by $(Z_{i1}, \dots, Z_{ip})_{1 \leq i \leq n}$ the resulting (topological) persistent vectors, i.e., the respective persistence values for each m/z value. The aim of the logistic regression is to model and estimate the effects of the available covariates on the conditional probability, $\pi_i = P(Y_i = 1 | Z_{i1}, \dots, Z_{ip})$, for the outcome $(Y_i)_{1 \leq i \leq n}$ and the numerical realizations of the covariates, i.e., $(Z_{ij})_{\substack{1 \leq i \leq n \\ 1 \leq j \leq p}}$. In this setting, the pairs $(Y_i, Z_{i1}, \dots, Z_{ip})_{1 \leq i \leq n}$ are assumed to be independent. LR models combine the probability π_i with the linear predictor η_i via a "structural" (functional) component given in the linear form $\pi_i = h(\eta_i) = h(\beta_0 + \beta_1 Z_{i1} + \dots + \beta_p Z_{ip})$ (for more details, see Section 2 in [36]).

In this study, we consider the logit (canonical) link function. Then, the logistic response function is given by,

$$\pi_i = h(\eta_i) = \frac{\exp(\eta_i)}{1 + \exp(\eta_i)}.$$

Correspondingly, the logit link function is given by

$$g(\pi_i) = \log\left(\frac{\pi_i}{1 - \pi_i}\right) = \beta_0 + \beta_1 Z_{i1} + \dots + \beta_p Z_{ip} = Z_i^T \beta. \quad (3)$$

Here, $\beta := (\beta_0, \beta_1, \dots, \beta_p)^T$ and $Z_i := (1, Z_{i1}, \dots, Z_{ip})$, where the first coordinate corresponds to an intercept term, and for $i \in \{1, \dots, n\}$. The unknown parameters are (usually) estimated by the maximum (log-) likelihood principle. The

log-likelihood function related to model (3) is expressed by

$$l(\beta) = \sum_{i=1}^n \{Y_i [\log(\pi_i) - \log(1 - (\pi_i))] + \log(1 - \pi_i)\}. \quad (4)$$

For the aforementioned (logit) model, by plugging

$$\pi_i = \frac{\exp(Z_i^T \beta)}{1 + \exp(Z_i^T \beta)} \quad \text{along with} \quad 1 - \pi_i = \frac{1}{1 + \exp(Z_i^T \beta)}$$

in (4), it yields that

$$l(\beta) = \sum_{i=1}^n \{Y_i (Z_i^T \beta) - \log(1 + \exp(Z_i^T \beta))\}. \quad (5)$$

Finally, the probability that an unobserved (new) observation is assigned to class 1 is estimated by substituting $(\beta_0, \dots, \beta_p)$ by their fitted values and the $(Z_j)_{1 \leq j \leq p+1}$ with their numerical realizations for the considered new observation in $P(Y = 1 | Z_1, \dots, Z_{p+1}) = \frac{\exp(Z^T \beta)}{1 + \exp(Z^T \beta)}$. Here, we have $p + 1$ covariates since the first coordinate corresponds to the intercept term. Respectively, the new observation is assigned to class $Y = 1$ if the conditional probability, $P(Y = 1) > c$, is greater than a pre-specified threshold c , and oppositely to class $Y = 0$. In this study, we set $c = 0.5$, a commonly used threshold (see [34]). To obtain the numerical results, we adopted the "LogisticRegression()" function in *scikit-learn*, v. 1.2.1 ([37]) (with no penalty) to obtain our numerical results.

Random Forest

The RF algorithm has become an established non-parametric procedure for regression and classification tasks. It has been broadly used in various scientific disciplines ([38], [39], [40]), including subtyping of lung cancer [41]. RF was originally introduced by Leo Breiman in [42] and presents an "ensemble learning" approach constituting the aggregation of a collection of a great number of decision trees ([43]). RF takes advantage of numerous decision trees, which leads to a reduction of empirical variance in comparison to a single (decision) tree and significant enhancements in its prediction accuracy ([35]). RF utilizes decision trees in order to calculate the majority votes in the leaf nodes when deciding a class label for each observational unit ([42], [35]). In essence, RF consists of two steps. The first step is to build an RF tree. The following step is to classify the data on the basis of an RF tree that has been generated in the first step. For an in-depth algorithmic scheme, we refer to [44] and [39].

In this study, we use the original variant of RF (see [42]), where each tree of the RF algorithm is constructed on a bootstrap sample drawn arbitrarily from the data by employing the classification and regression trees method and minimizes the Gini impurity (GI) regarding the splitting criterion. When constructing each tree (for each split), solely a pre-specified number of randomly selected (data) covariates are deemed as candidates for splitting.

An important step when using RF is selecting hyperparameters, also called tuning parameters. Their values have to be optimized attentively since the optimal quantities depend on the data at hand. An essential concept regarding tuning optimization is "overfitting". Namely, tuning values corresponding to sophisticated rules tend to "overfit" the training data set. As a result, they produce prediction rules too precise to the training set and perform pretty well for this data but likely not that good for independent data. As discussed in [45], the choice of less-than-optimal parameter quantities can be (at least) partially prevented by utilizing a test set or cross-validation (CV) procedures for tuning. However, it is out of the scope of this study to identify the (most) optimal tuning parameters in the context of MALDI classification. Instead, we are predominantly interested in evaluating the performance of the proposed TDA approach to the MALDI data set. To this end, we select the "typical default values" for classification in the context of RF, which are given in Table 1 in [45]. Specifically, we set in our numerical experiments the tuning parameters as follows: the number of trees is equal to 500. The number of drawn candidate variables per split is equal to \sqrt{p} (often referred to as "mtry", *max_depth* in *scikit-learn*). The splitting criterion in the nodes is the gini impurity. The minimum number of samples in a terminal node is equal to one (*min_samples_leaf* in *scikit-learn*). The samples are drawn with replacement when generating trees, i.e., we bootstrap each tree, and the seed for all experiments was set to 1234.

We carried out the RF approach on the basis of the resulting algebraic vectors $Z_i = (Z_{i1}, \dots, Z_{ip})_{1 \leq i \leq n}$ and the binary outcome $(Y_i)_{1 \leq i \leq n}$. Notice that a unit vector has not been considered, i.e., without an intercept term, as in the case of LR. We adopted the function '*RandomForestClassifier()*' in [37] (*version 1.2.1*) to yield the numerical results.

Real Data Analysis

Description of the MALDI-IMS data

This section presents the empirical results obtained by carrying out different classification schemes, based on different levels of persistence extraction, to MALDI-IMS data. In particular, this data set has been employed in several preceding studies (cf. [4], [6], [9], [7], and [10]). We refer to [4], [7], and [9] for an in-depth description of the aforementioned data set concerning its acquisition protocols, tissue sections, tissue blocks, etc. Here, we provide only a brief outline of the data set.

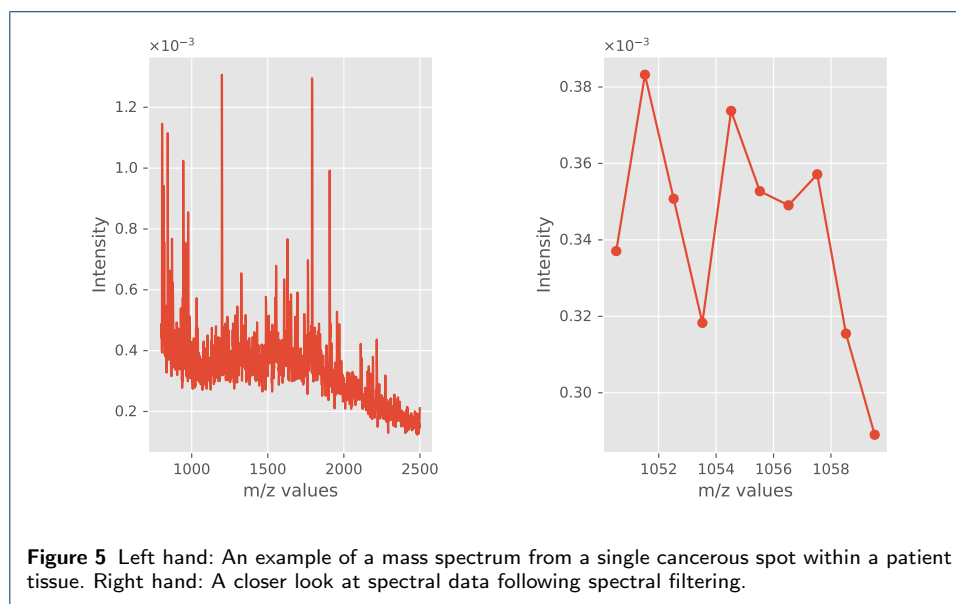
Cylindrical tissue cores (CTCs) of non-small cell lung cancer were taken from 304 patients. Specifically, 168 patients were associated with primary lung adenocarcinoma (ADC), while 136 patients were associated with primary squamous cell carcinoma (SqCC). CTCs of all patients were gathered into eight tissue microarray (TMA) blocks (for a closer look at each TMA, see Table 1). As discussed in the supplement of [9], the tumor status and subtyping for all CTCs were affirmed by standard "histopathological examination". Furthermore, this data set has been generated only on annotated subregions called regions-of-interest (cf. [6]), i.e., subregions comprising only tumor cells. Following measurement, the raw MALDI data were combined into a joint data set through the SCiLS LAB (version 2016b, Bruker Daltonik). Accompanied by the software's default baseline correction, total ion count (TIC) normalization was carried out (for more details, see [5], [10]). For

the follow-up data processing, the data was loaded into MATLAB (version 2016B, Mathworks), where spectral filtering of 0.4 Dalton (unit) width was applied. Concretely, the latter data-processing step centers m/z values around expected peptide masses (for more details, see [9]).

For illustrative purposes, Figure 5 depicts an example of an output from a MALDI experiment taken from a single spatial location in the provided tissue. In the left panel of Figure 5, the m/z -values are illustrated on the x-axis, while the intensity values of "ionizable molecules" are charted on the vertical axis. Respectively this spatial information can be used in two directions, namely, for the determination of the subtyping (i.e., the cancer subtypes) or the identification of the source of the tumor in tissue. The right panel of Figure 5 illustrates the data granularity following spectral filtering.

As pointed out in different studies (e.g., [46], [47]), LC is the primary cause of cancer-related fatalities globally; for example, there were 1.59 million reported deaths in 2012 (see [47]). Two major LC categories are recognized, i.e., small cell lung cancer (SCLC) and non-small cell lung cancer (NSLC). The latter constitutes approximately 85% of all LC cases as reported ([47], [46]). The two prevailing NSLC entities are ADC and SqCC, compromising approx. 50% and 40% of all lung-related cancers, respectively ([46], [47]). As pointed out, e.g., in [9] (*supplement* Appendix D), the distinction between these two common subtypes is of great importance for the therapy choice of patients. Throughout this study, the number of spectra is $n = 4667$ (observational units) and the number of m/z values is $p = 1699$.

Briefly put, we applied the proposed framework based on standard data-processing steps. The analyzed data is publicly available in Gitlab, provided in [9]. Remark we did not apply any additional data-processing steps.



Classification evaluation

To evaluate the performance of the classification schemes, we mimic the realistic scenario proposed in [9]. Namely, the data is split into training and test sets. The

Table 1 Descriptive statistics for each TMA

TMA	Number of spectra	Ratio ADC: SqCC
TMA_1	680	59.3 %
TMA_2	437	60.4 %
TMA_3	563	41.2 %
TMA_4	601	49.3 %
TMA_5	512	63.5 %
TMA_6	650	76.8 %
TMA_7	536	50.4 %
TMA_8	690	54.3 %

upcoming results were derived by performing k-fold cross-validation (CV) on a TMA level. Namely, from the overall set of eight TMA blocks, eight distinct test subsets were created based on each TMA. Then, in each of the eight CV folds, each classification scheme was applied to seven TMAs and predicted on the remaining test set —not considered in the training process. Finally, we reported the obtained results across all test sets.

The classification accuracy was assessed by computing the balanced accuracy. The latter metric is computed as the average proportions of correctly classified spectra for each class separately. As a result, this metric is independent with respect to imbalanced binary categories, i.e., when one of the target classes appears far more often than the other in the test set. To illustrate the numerical performances appertaining to the peak extraction level, we set a tuning parameter k based on different percentages of peak extraction.

Data-analysis results

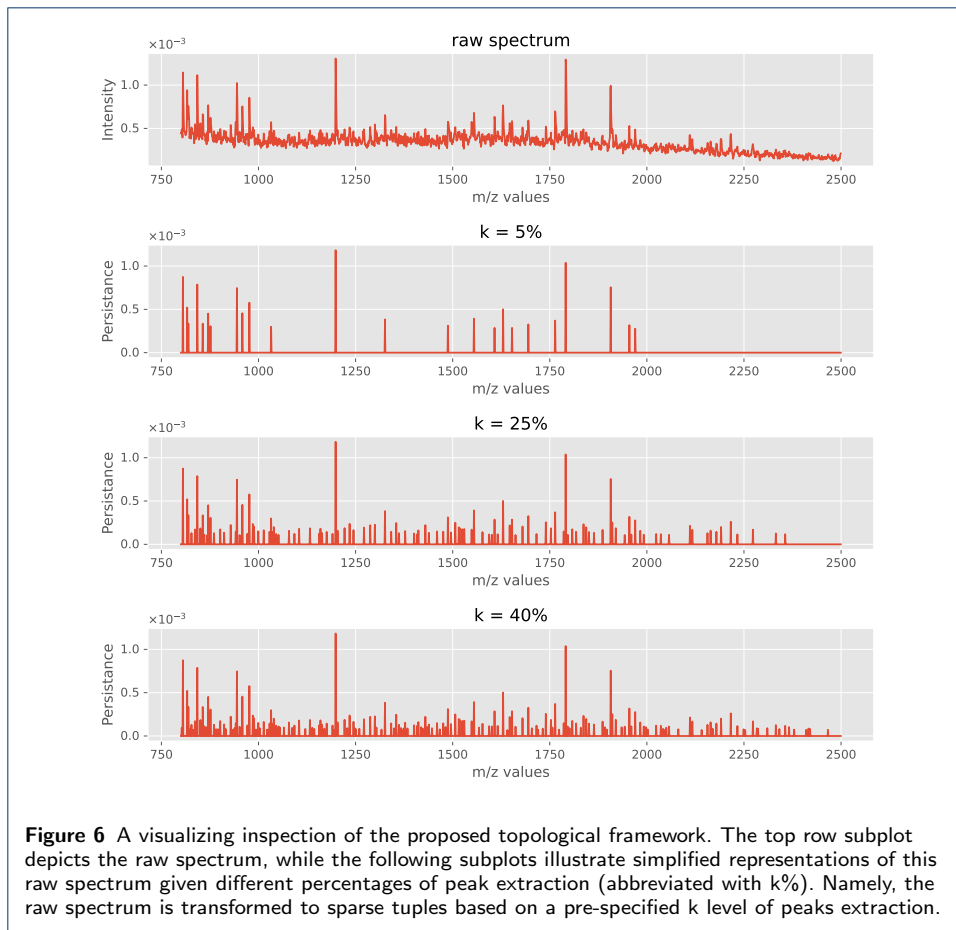
Statistic	k = 1%	k = 5%	k = 10%	k = 20%	k = 25%	k = 40%	k = 50%	raw data
mean	0.637	0.735	0.849	0.851	0.850	0.864	0.859	0.871
min	0.489	0.597	0.763	0.755	0.741	0.762	0.728	0.718
max	0.796	0.872	0.957	0.960	0.944	0.942	0.929	0.941
median	0.621	0.723	0.853	0.852	0.860	0.878	0.877	0.891
std	0.100	0.101	0.068	0.076	0.076	0.072	0.073	0.075

Table 2 Comparison table of 8-fold cross-validation. The table tabulates the obtained balanced accuracy results given different percentages of peak extraction and non-extracted data based on the LR classifier.

Statistic	k = 1%	k = 5%	k = 10%	k = 20%	k = 25%	k = 40%	k = 50%	raw data
mean	0.652	0.783	0.823	0.858	0.865	0.883	0.875	0.872
min	0.568	0.683	0.670	0.756	0.753	0.784	0.778	0.775
max	0.839	0.876	0.930	0.952	0.946	0.952	0.935	0.939
median	0.608	0.801	0.852	0.874	0.883	0.904	0.895	0.885
std	0.101	0.076	0.09	0.07	0.07	0.065	0.062	0.065

Table 3 Comparison table of 8-fold cross-validation. The table tabulates the obtained balanced accuracy results given different percentages of peak extraction and non-extracted data based on the RF classifier.

Figure 6 displays an example of the proposed topological feature extraction. Namely, the top row illustrates a raw spectrum (cf. Figure 5), whereas the next



subplots illustrate extracted persistence values. Here, the m/z values are plotted on the horizontal axes, while the vertical axes illustrate the derived persistence values, not the intensity values.

Tables 2 - 3 summarize the classification results obtained by running LR and RF classifiers based on several levels of the extracted persistence vectors. In both tables, the first columns contain the information on which statistical metric is illustrated in each row. Specifically, we report the metrics *mean* and *median* in order to evaluate the overall classification performance for each classification scheme. Furthermore, we also investigate the performance variation across the 8-folds. To this end, the metrics *min* and *max* are given. We abbreviate with "raw data" the non-extracted MALDI data, i.e., where the proposed persistence transformation was not applied. In comparison, the percentage of extracted persistence used for the evaluation, denoted by " k ", ranges in a grid of pre-specified percentages — $k \in \{1\%, 5\%, 10\%, 20\%, 25\%, 40\%, 50\%\}$.

Table 2 compares the numerical results (i.e., the balanced accuracy) obtained from the LR method. From here, it can be seen that the best numerical result is yielded on the raw data compared to the algebraic counterparts. Furthermore, we did not observe any gain in the running time of the cross-validation process between the raw data and the extracted algebraic counterparts.

Table 3 summarizes the numerical results obtained from the RF classifier. The best numerical results among all the empirical experiments are yielded on $k = 40\%$ persistence extraction and the RF classifier across all the metrics. Both overall performance metrics are the highest, i.e., the mean is 88.3% while the median is 90.4%, and also, they produced the highest values in terms of classification variation (their min or max values). Furthermore, we observed a significant gain in running time for the RF classifier when utilizing the algebraic versions. Specifically, the running time of the cross-validation process when $k = 25\%$ is appr. 3 minutes and appr. 4 minutes in the case of $k = 40\%$. In contrast, the running time for the raw data is appr. 16 minutes on a standard PC desktop.

As pointed out in [45], the number of trees is not a tunable parameter in "the classical sense". However, it has to be determined as "sufficiently high". To this end, we also executed the same tuning scheme where the number of trees was set to 1000 (the full table is given in the provided GitHub link). The numerical results for the best topological performer (i.e., $k = 40\%$, the mean is 88.3 %) and the non-extracted counterpart (the mean is 87.5 %) have changed slightly. However, the running time for the CV process has altered significantly because the computational time for RF rises linearly with the number of trees (see [45]).

Discussion

Summary

Motivated by the MALDI classification studies, the objective of this study has been to propose a novel custom-made approach for modeling MALDI-IMS data. In general, the study's methodology consists of two steps. First, we carry out the introduced topological framework to obtain the intrinsic information from each mass spectrum, given thousands of m/z values. Generally speaking, this step can be considered a tailor-made (unsupervised) feature extraction for MALDI-IMS data. Second, we execute two supervised classification methods based on the resulting persistence vectors so as to classify the observational units into lung cancer subtypes.

The usefulness of the proposed topological framework consists of two perspectives. First and foremost, our numerical results illustrate that the topological framework extracts the necessary information, which can be utilized for further classification tasks. The obtained results are competitive with other data-analysis methods for this data set (cf. [9]). Second, the proposed framework compresses MALDI-IMS data, resulting in a significant computational gain for the RF classifier. In addition, this framework processes the peak information from each mass spectrum individually. Namely, this allows the utilization of already trained classifiers (e.g., from this study) to unseen data from different sources (e.g., laboratories). We show that our topological framework can be adopted in a computationally efficient algorithm depending on a single tuning parameter, i.e., the fraction of used peaks.

Outlook

The persistence transformation is a novel tool for topological data analysis, which can be employed in different real-world applications. Future work to extend the introduced framework might include the application of the heat equation to reduce the impact of noisy peaks (see [24]), which might increase the classification performance. Alternatively, one can use the persistence pairs as input points for a second

persistence homology analysis. However, any computational improvement would lead to the extension of the computational time. Furthermore, the information on the position of the peaks might be used for backtracking to identify (biologically) relevant molecules given as peaks. Finally, the algorithm used in this paper shows similarity to Morse Theory ([48]) and especially to the matching theorems in [20]. This presents an interesting topic for follow-up research.

Appendix

Proof of Theorem 1: The algorithm to calculate the reduced persistence transformation is divided into two parts: the recursion start (Algorithm 1) and the recursion step (Algorithm 2).

Algorithm 1 Recursion start

```

1: Input:  $[f(x_0), \dots, f(x_n)]$ 
2: Return:  $[(\hat{x}, p(\hat{x})), \dots]$ 
3:  $\text{maxima}, \text{minima}, \text{featurePairs} \leftarrow \emptyset$ 
4: for all  $x_i \in [x_0, x_n]$  do
5:   if  $x_i$  is maximum then
6:      $\text{maxima} \leftarrow (x_i, f(x_i))$ 
7:   else if  $x_i$  is minimum then
8:      $\text{minima} \leftarrow (x_i, f(x_i))$ 
9:    $\text{SORT}(\text{maxima}, f(x), >)$ 
10:   $\text{SORT}(\text{minima}, f(x), <)$ 
11:   $(\hat{x}, f(\hat{x})) \leftarrow \text{maxima.pop}(0)$ 
12:   $\text{featurePairs} \leftarrow (\hat{x}, f(\hat{x}) - \text{minima}[0][1])$ 
13:   $\text{RecursionStep}(x_0, \hat{x}, \text{maxima.copy}(), \text{minima.copy}(), \text{featurePairs})$ 
14:   $\text{RecursionStep}(x_n, \hat{x}, \text{maxima.copy}(), \text{minima.copy}(), \text{featurePairs})$ 
15: return  $\text{featurePairs}$ 

```

The *recursion start* (Algorithm 1) gets as input the list of all the intensity values for each m/z value, marked as $f(x_i)$. Let m be the number of maxima in this spectra. In the beginning, empty lists are created for the maxima, the minima, and the results (called "featurePairs"). The latter list stores the x value, i.e., the position, as well as the persistence of each peak. Notice that each recursion step updates the list instead of returning results.

In the next step, all the minima and the maxima are stored in the corresponding lists in tuples of the form $(x, f(x))$. For this, the algorithm iterates through the list of the $f(x_i)$. If the value is larger than its neighbors, it is marked as maximum and stored in the corresponding list. Correspondingly, values that are smaller than their neighbors are marked as a minimum. This identification of extremal points can be made in linear run-time since the list is traversed just once, resulting in a complexity of $\sigma(n)$. The two lists *maxima* and *minima* are then sorted by their corresponding value $f(x_i)$ (the *minima* list inverted) with a complexity of $\sigma(m \cdot \log m)$.

For the largest feature, the global maximum, the persistence is defined to be the difference to the global minimum (see Equation (1)). These values are the first elements of their corresponding lists. After calculating the persistence, the maximum is removed from the list, and the found feature $(x, p(x))$ is stored in the list *persistencePairs*. The *recursion step* is called afterwards with the intervals $[x_0, \hat{x})$ and (x_n, \hat{x}) . Notice that the second interval is reversed. As input, the *recursion step* gets a copy of the two lists minima and maxima as well as the original list *featurePairs*. All these computations can be done in constant time, i.e., $\sigma(1)$. After the last *recursion step*, all the features are detected and stored in the *featurePairs* list and can be returned.

Algorithm 2 Recursion Step

```

1: Input: start, end, maxima, minima, featurePairs
2: for all  $(x_i, f(x_i)) \in \text{maxima}$  do
3:   if  $x_i \notin [\text{start}, \text{end}]$  then
4:      $\text{maxima} \leftarrow \text{maxima} \setminus (x_i, f(x_i))$ 
5:   if  $|\text{maxima}| = 0$  then
6:     return
7:    $(\hat{x}, f(\hat{x})) \leftarrow \text{maxima.pop}(0)$ 
8:   RecursionStep(start,  $\hat{x}$ , maxima.copy(), minima.copy(), featurePairs)
9:   for all  $(x_i, f(x_i)) \in \text{minima}$  do
10:    if  $x_i \notin (\hat{x}, \text{end})$  then
11:       $\text{minima} \leftarrow \text{minima} \setminus (x_i, f(x_i))$ 
12:     $(x', f(x')) \leftarrow \text{minima.pop}(0)$ 
13:    featurePairs  $\leftarrow (\hat{x}, f(\hat{x}) - f(x'))$ 
14:    RecursionStep( $x'$ ,  $\hat{x}$ , maxima.copy(), minima.copy(), featurePairs)
15:    RecursionStep( $x'$ , end, maxima.copy(), minima.copy(), featurePairs)

```

The input for the *recursion step* (Algorithm 2) consists of two indices, namely *start* and *end* (indicating the part of the data which is processed in the current recursion step, i.e., the positions of m/z values), a list of *maxima* and a list of *minima*, and the shared list of *featurePairs*. In the first step, the routine removes all the maxima not in the currently processed part of the data. There are at most m elements in the *maximum* list, so the complexity of this task is $\sigma(m)$. If the list is empty after the removing step, the *recursion step* reaches the end and can return. If not, it removes the first element \hat{x} from the list. This is the most persistent feature (in terms of topology) in the processed part of the data. The elder rule (cf. [26]) states that the feature can only merge with a feature with a larger persistence, which is per construction at the index *end*. The corresponding minimum (cf. Equation (2)) to \hat{x} can only be in the interval (\hat{x}, end) so the *minima* list can be filtered in a similar fashion to the *maxima* list with the same complexity. Since there are more possible features in the interval (start, \hat{x}) , the *recursion step* is called once more for this interval.

The values \hat{x} and the smallest minimum x' from the *minima* list generate a topological feature. This feature is updated in the original *featurePairs* list, and the recursion step can be repeated with the two intervals (x', \hat{x}) and (x', end) .

The recursion step is processed at least once for each maximum with three extra calls after no more maxima are left, i.e., it runs at most $4 \times m$ times. Given the complexity of each step of $\sigma(m)$, the complexity of all the recursion steps together is $\sigma(m^2)$. This gives an overall complexity of the algorithm of

$$\sigma(n) + \sigma(m^2) + \sigma(m \cdot \log m) = \sigma(n) + \sigma(m^2).$$

For each maximum, there is a tuple stored which contains the information of the position and the persistence, resulting in an overall storage use of $2m$ elements.

The algorithm always terminates since, at each recursion step, one maximum is removed from the list of maxima—if it is not already empty. Likewise, each part of the input list is being processed. Since there is only a finite number of elements in the *maxima* list (i.e., m), the algorithm terminates after all are processed. Even more, the algorithm returns all the features with their persistence. Each maximum creates a feature, and all maxima are processed. They are paired with the correct minimum between themselves and a feature with a higher persistence according to

the elder rule (see [26]). Hence, the algorithm always terminates and returns the correct solution in $\sigma(n) + \sigma(m^2)$ run-time. \square

Acknowledgements

The authors extend their sincere gratitude to Prof. Dmitry Feichtner-Kozlov and Prof. Thorsten Dickhaus at the University of Bremen for supervising GK and VV. Also, we sincerely thank Lena Ranke, Friederike Preusse, and Lukas Mentz for their constructive criticism of the manuscript. The financial support by the German Research Foundation via the RTG 2224, titled " π^3 : Parameter Identification - Analysis, Algorithms, Implementations" is gratefully acknowledged.

Funding

Deutsche Forschungsgemeinschaft. Grant Number: RTG 2224

Availability of data and materials

Python code with the numerical results presented in the paper, including the MALDI data, is available in: <https://github.com/klailag/SupervisedTDAMethodForMALDI>

DECLARATIONS

Ethics approval and consent to participate

Not applicable.

Competing interests

The authors declare that they have no competing interests.

Consent for publication

Not applicable.

Authors' contributions

This paper is based on joined work of the three main authors as equal contributors. GK implemented the algorithm and proved the complexity. VV took care of the classifiers and the statistical interpretation of the results. AS helped clarify the notion of persistent transformation and its connection to the persistence diagram via the elder rule and proposed examples illustrating this connection. All authors have written the manuscript and approved the final version.

Authors' information

- Gideon Klaila, klailag@uni-bremen.de
- Vladimir Vutov, vkutov@uni-bremen.de
- Anastasios Stefanou, stefanou@uni-bremen.de

Author details

¹Institute for Algebra, Geometry, Topology and their Applications (ALTA); Department of Mathematics, University of Bremen, 28359 Bremen, Germany. ²Institute for Statistics, Department of Mathematics; Department of Mathematics University of Bremen, 28359 Bremen, Germany.

References

1. Mortier, T., Wieme, A.D., Vandamme, P., Waegeman, W.: Bacterial species identification using maldi-tof mass spectrometry and machine learning techniques: A large-scale benchmarking study. *Computational and Structural Biotechnology Journal* **19**, 6157–6168 (2021). doi:[10.1016/j.csbj.2021.11.004](https://doi.org/10.1016/j.csbj.2021.11.004)
2. Caprioli, R.M., Farmer, T.B., Gile, J.: Molecular imaging of biological samples: localization of peptides and proteins using MALDI-TOF MS. *Analytical chemistry* **69** **23**, 4751–60 (1997)
3. Alexandrov, T., Bartels, A.: Testing for presence of known and unknown molecules in imaging mass spectrometry. *Bioinformatics (Oxford, England)* **29**(18), 2335–2342 (2013). doi:[10.1093/bioinformatics/btt388](https://doi.org/10.1093/bioinformatics/btt388)
4. Boskamp, T., Lachmund, D., Oetjen, J., Cordero Hernandez, Y., Trede, D., Maass, P., Casadonte, R., Kriegsmann, J., Warth, A., Dienemann, H., Weichert, W., Kriegsmann, M.: A new classification method for MALDI imaging mass spectrometry data acquired on formalin-fixed paraffin-embedded tissue samples. *Biochim Biophys Acta Proteins Proteom* **1865**(7), 916–926 (2017). doi:[10.1016/j.bbapap.2016.11.003](https://doi.org/10.1016/j.bbapap.2016.11.003)
5. Alexandrov, T.: MALDI imaging mass spectrometry: statistical data analysis and current computational challenges. *BMC Bioinformatics* **13** **Suppl 16**, 11 (2012). doi:[10.1186/1471-2105-13-S16-S11](https://doi.org/10.1186/1471-2105-13-S16-S11)
6. Behrmann, J., Etmann, C., Boskamp, T., Casadonte, R., Kriegsmann, J., Maaß, P.: Deep learning for tumor classification in imaging mass spectrometry. *Bioinform.* **34**(7), 1215–1223 (2018). doi:[10.1093/bioinformatics/btx724](https://doi.org/10.1093/bioinformatics/btx724)
7. Kriegsmann, J., Kriegsmann, M., Casadonte, R.: MALDI TOF imaging mass spectrometry in clinical pathology: a valuable tool for cancer diagnostics (review). *Int J Oncol* **46**(3), 893–906 (2015). doi:[10.3892/ijo.2014.2788](https://doi.org/10.3892/ijo.2014.2788)
8. Veselkov, K.A., Mirnezami, R., Strittmatter, N., Goldin, R.D., Kinross, J., Speller, A.V.M., Abramov, T., Jones, E.A., Darzi, A., Holmes, E., Nicholson, J.K., Takats, Z.: Chemo-informatic strategy for imaging mass spectrometry-based hyperspectral profiling of lipid signatures in colorectal cancer. *Proceedings of the National Academy of Sciences* **111**(3), 1216–1221 (2014). doi:[10.1073/pnas.1310524111](https://doi.org/10.1073/pnas.1310524111)
9. Leuschner, J., Schmidt, M., Fernsel, P., Lachmund, D., Boskamp, T., Maass, P.: Supervised non-negative matrix factorization methods for MALDI imaging applications. *Bioinformatics* **35**(11), 1940–1947 (2019). doi:[10.1093/bioinformatics/bty909](https://doi.org/10.1093/bioinformatics/bty909)

10. Vutov, V., Dickhaus, T.: Multiple two-sample testing under arbitrary covariance dependency with an application in imaging mass spectrometry. *Biometrical Journal* **65**(2), 2100328 (2023)
11. Wijetunge, C.D., Saeed, I., Boughton, B.A., Roessner, U., Halgamuge, S.K.: A new peak detection algorithm for MALDI mass spectrometry data based on a modified Asymmetric Pseudo-Voigt model. *BMC Genomics* **16 Suppl 12**, 12 (2015). doi:[10.1186/1471-2164-16-S12-S12](https://doi.org/10.1186/1471-2164-16-S12-S12)
12. Timm, W., Scherbart, A., Böcker, S., Kohlbacher, O., Nattkemper, T.W.: Peak intensity prediction in MALDI-TOF mass spectrometry: A machine learning study to support quantitative proteomics. *BMC Bioinform.* **9** (2008). doi:[10.1186/1471-2105-9-443](https://doi.org/10.1186/1471-2105-9-443)
13. Yang, C., He, Z., Yu, W.: Comparison of public peak detection algorithms for MALDI mass spectrometry data analysis. *BMC Bioinform.* **10** (2009). doi:[10.1186/1471-2105-10-4](https://doi.org/10.1186/1471-2105-10-4)
14. Lieb, F., Boskamp, T., Stark, H.G.: Peak detection for maldi mass spectrometry imaging data using sparse frame multipliers. *Journal of Proteomics* **225**, 103852 (2020). doi:[10.1016/j.jprot.2020.103852](https://doi.org/10.1016/j.jprot.2020.103852)
15. Slawski, M., Hussong, R., Tholey, A., Jakoby, T., Gregorius, B., Hildebrandt, A., Hein, M.: Isotope pattern deconvolution for peptide mass spectrometry by non-negative least squares/least absolute deviation template matching. *BMC Bioinform.* **13**, 291 (2012). doi:[10.1186/1471-2105-13-291](https://doi.org/10.1186/1471-2105-13-291)
16. von Schroeder, J.: Stable Feature Selection with Applications to MALDI Imaging Mass Spectrometry Data. Preprint, available via <https://arxiv.org/abs/2006.15077>. (2020)
17. Vutov, V., Dickhaus, T.: Multiple multi-sample testing under arbitrary covariance dependency. arXiv preprint arXiv:2202.12347 (2022)
18. Otter, N., Porter, M.A., Tillmann, U., Grindrod, P., Harrington, H.A.: A roadmap for the computation of persistent homology. *EPJ Data Sci.* **6**(1), 17 (2017). doi:[10.1140/epjds/s13688-017-0109-5](https://doi.org/10.1140/epjds/s13688-017-0109-5)
19. Chazal, F., Michel, B.: An introduction to topological data analysis: Fundamental and practical aspects for data scientists. *Frontiers Artif. Intell.* **4**, 667963 (2021). doi:[10.3389/frai.2021.667963](https://doi.org/10.3389/frai.2021.667963)
20. Kozlov, D.N.: A combinatorial method to compute explicit homology cycles using discrete morse theory. *J. Appl. Comput. Topol.* **4**(1), 79–100 (2020). doi:[10.1007/s41468-019-00042-x](https://doi.org/10.1007/s41468-019-00042-x)
21. Skaf, Y., Laubenbacher, R.C.: Topological data analysis in biomedicine: A review. *J. Biomed. Informatics* **130**, 104082 (2022). doi:[10.1016/j.jbi.2022.104082](https://doi.org/10.1016/j.jbi.2022.104082)
22. Bukkuri, A., Andor, N., Darcy, I.K.: Applications of topological data analysis in oncology. *Frontiers Artif. Intell.* **4**, 659037 (2021). doi:[10.3389/frai.2021.659037](https://doi.org/10.3389/frai.2021.659037)
23. Loughrey, C.F., Fitzpatrick, P., Orr, N., Jurek-Loughrey, A.: The topology of data: opportunities for cancer research. *Bioinform.* **37**(19), 3091–3098 (2021). doi:[10.1093/bioinformatics/btab553](https://doi.org/10.1093/bioinformatics/btab553)
24. Weis, C., Horn, M., Rieck, B., Cuénod, A., Egli, A., Borgwardt, K.M.: Topological and kernel-based microbial phenotype prediction from MALDI-TOF mass spectra. *Bioinform.* **36**(Supplement-1), 30–38 (2020). doi:[10.1093/bioinformatics/btaa429](https://doi.org/10.1093/bioinformatics/btaa429)
25. Fernsel, P.: Spatially coherent clustering based on orthogonal nonnegative matrix factorization. *Journal of Imaging* **7**(10), 194 (2021)
26. Edelsbrunner, H., Harer, J.L.: *Computational Topology: an Introduction*. American Mathematical Society, Providence, USA (2010)
27. Fasy, B., Lecci, F., Rinaldo, A., Wasserman, L., Balakrishnan, S., Singh, A.: Statistical inference for persistent homology: Confidence sets for persistence diagrams (2013). doi:[10.1214/14-AOS1252](https://doi.org/10.1214/14-AOS1252)
28. Edelsbrunner, H., Letscher, D., Zomorodian, A.: Topological persistence and simplification. *Discret. Comput. Geom.* **28**(4), 511–533 (2002). doi:[10.1007/s00454-002-2885-2](https://doi.org/10.1007/s00454-002-2885-2)
29. Cohen-Steiner, D., Edelsbrunner, H., Harer, J.: Stability of persistence diagrams. *Discret. Comput. Geom.* **37**(1), 103–120 (2007). doi:[10.1007/s00454-006-1276-5](https://doi.org/10.1007/s00454-006-1276-5)
30. Vlontzos, A., Cao, Y., Schmidtke, L., Kainz, B., Monod, A.: Topological data analysis of database representations for information retrieval. *CoRR abs/2104.01672* (2021). [2104.01672](https://arxiv.org/abs/2104.01672)
31. Grélard, F., Legland, D., Fanuel, M., Arnaud, B., Foucat, L., Rogniaux, H.: Esmraldi: efficient methods for the fusion of mass spectrometry and magnetic resonance images. *BMC Bioinform.* **22**(1), 56 (2021). doi:[10.1186/s12859-020-03954-z](https://doi.org/10.1186/s12859-020-03954-z)
32. Contessoto, M., Mémoli, F., Stefanou, A., Zhou, L.: Persistent cup-length. arXiv preprint arXiv:2107.01553 (2021)
33. Mémoli, F., Stefanou, A., Zhou, L.: Persistent cup product structures and related invariants. arXiv preprint arXiv:2211.16642 (2022)
34. Couronné, R., Probst, P., Boulesteix, A.: Random forest versus logistic regression: a large-scale benchmark experiment. *BMC Bioinform.* **19**(1), 270–127014 (2018). doi:[10.1186/s12859-018-2264-5](https://doi.org/10.1186/s12859-018-2264-5)
35. Kirasich, K., Smith, T., Sadler, B.: Random forest vs logistic regression: binary classification for heterogeneous datasets. *SMU Data Science Review* **1**(3), 9 (2018)
36. Fahrmeir, L., Tutz, G., Hennevogel, W., Salem, E.: *Multivariate Statistical Modelling Based on Generalized Linear Models* vol. 425. Springer, Berlin, Germany (1994)
37. Pedregosa, F., Varoquaux, G., Gramfort, A., Michel, V., Thirion, B., Grisel, O., Blondel, M., Prettenhofer, P., Weiss, R., Dubourg, V., Vanderplas, J., Passos, A., Cournapeau, D., Brucher, M., Perrot, M., Duchesnay, E.: Scikit-learn: Machine learning in Python. *Journal of Machine Learning Research* **12**, 2825–2830 (2011)
38. Pal, M.: Random forest classifier for remote sensing classification. *International journal of remote sensing* **26**(1), 217–222 (2005)
39. Noshad, Z., Javaid, N., Saba, T., Wadud, Z., Saleem, M.Q., Alzahrani, M.E., Sheta, O.E.: Fault detection in wireless sensor networks through the random forest classifier. *Sensors* **19**(7), 1568 (2019). doi:[10.3390/s19071568](https://doi.org/10.3390/s19071568)
40. Shrestha, B., Stephen, H., Ahmad, S.: Impervious surfaces mapping at city scale by fusion of radar and optical data through a random forest classifier. *Remote. Sens.* **13**(15), 3040 (2021). doi:[10.3390/rs13153040](https://doi.org/10.3390/rs13153040)
41. Neumann, J.M., Freitag, H., Hartmann, J.S., Niehaus, K., Galanis, M., Griesshammer, M., Kellner, U., Bednarz, H.: Subtyping non-small cell lung cancer by histology-guided spatial metabolomics. *Journal of cancer research and clinical oncology* **148**(2), 351–360 (2022)

42. Breiman, L.: Random forests. *Machine learning* **45**(1), 5–32 (2001)
43. Hastie, T., Tibshirani, R., Friedman, J.H.: *The Elements of Statistical Learning: Data Mining, Inference, and Prediction*, 2nd Edition. Springer Series in Statistics. Springer, New York, NY (2009). doi:[10.1007/978-0-387-84858-7](https://doi.org/10.1007/978-0-387-84858-7). <https://doi.org/10.1007/978-0-387-84858-7>
44. Liaw, A., Wiener, M., *et al.*: Classification and regression by randomforest. *R news* **2**(3), 18–22 (2002)
45. Probst, P., Wright, M.N., Boulesteix, A.: Hyperparameters and tuning strategies for random forest. *WIREs Data Mining Knowl. Discov.* **9**(3) (2019). doi:[10.1002/widm.1301](https://doi.org/10.1002/widm.1301)
46. Sugár, S., Bugyi, F., Tóth, G., Pápay, J., Kovalszky, I., Tornóczy, T., Drahos, L., Turiák, L.: Proteomic analysis of lung cancer types - a pilot study. *Cancers* **14**(11) (2022). doi:[10.3390/cancers14112629](https://doi.org/10.3390/cancers14112629)
47. Kriegsmann, M., Casadonte, R., Kriegsmann, J., Dienemann, H., Schirmacher, P., Hendrik Kobarg, J., Schwamborn, K., Stenzinger, A., Warth, A., Weichert, W.: Reliable Entity Subtyping in Non-small Cell Lung Cancer by Matrix-assisted Laser Desorption/Ionization Imaging Mass Spectrometry on Formalin-fixed Paraffin-embedded Tissue Specimens. *Mol Cell Proteomics* **15**(10), 3081–3089 (2016). doi:[10.1074/mcp.m115.057513](https://doi.org/10.1074/mcp.m115.057513)
48. Milnor, J.: *Morse Theory*. (AM-51), Volume 51. Princeton University Press, Princeton (1963). doi:[10.1515/9781400881802](https://doi.org/10.1515/9781400881802). <https://doi.org/10.1515/9781400881802>